A machine learning approach to investigate the relationship between shape features and numerically predicted risk of ascending aortic aneurysm

Article *in* Biomechanics and Modeling in Mechanobiology · October 2017

DOI: 10.1007/s10237-017-0903-9

Biomech Model Mechanobiol
DOI 10.1007/s10237-017-0903-9

ORIGINAL PAPER

A machine learning approach to investigate the relationship between shape features and numerically predicted risk of ascending aortic aneurysm

Liang Liang[1] · **Minliang Liu**[1] · **Caitlin Martin**[1] · **John A. Elefteriades**[2] · **Wei Sun**[1]

Received: 14 June 2016 / Accepted: 27 March 2017

Abstract Geometric features of the aorta are linked to patient risk of rupture in the clinical decision to electively repair an ascending aortic aneurysm (AsAA). Previous approaches have focused on relationship between intuitive geometric features (e.g., diameter and curvature) and wall stress. This work investigates the feasibility of a machine learning approach to establish the linkages between shape features and FEA-predicted AsAA rupture risk, and it may serve as a faster surrogate for FEA associated with long simulation time and numerical convergence issues. This method consists of four main steps: (1) constructing a statistical shape model (SSM) from clinical 3D CT images of AsAA patients; (2) generating a dataset of representative aneurysm shapes and obtaining FEA-predicted risk scores defined as systolic pressure divided by rupture pressure (rupture is determined by a threshold criterion); (3) establishing relationship between shape features and risk by using classifiers and regressors; and (4) evaluating such relationship in cross-validation. The results show that SSM parameters can be used as strong shape features to make predictions of risk scores consistent with FEA, which lead to an average risk classification accuracy of 95.58% by using support vector machine and an average regression error of 0.0332 by using support vector regression, while intuitive geometric features have relatively weak performance. Compared to FEA, this machine learning approach is magnitudes faster. In our future studies, material properties and inhomogeneous thickness will be incorporated into the models and learning algorithms, which may lead to a practical system for clinical applications.

Keywords Ascending aortic aneurysm · Finite element analysis · Computer-aided diagnosis · Machine learning

Liang Liang and Minliang Liu have contributed equally to this work, and should be considered as co-first authors.

✉ Wei Sun
wei.sun@bme.gatech.edu

1 Tissue Mechanics Laboratory, The Wallace H. Coulter Department of Biomedical Engineering, Georgia Institute of Technology and Emory University, Technology Enterprise Park, Room 206 387 Technology Circle, Atlanta, GA 30313-2412, USA

2 Aortic Institute of Yale-New Haven Hospital, Yale University, New Haven, CT, USA

1 Introduction

Thoracic aortic aneurysm (TAA), which may lead to aortic rupture or dissection, is a lethal disease: the five-year survival in patients left untreated is 54%, and ascending aortic aneurysm (AsAA) is substantially more common compared to other types of TAA (Davies et al. 2002). Symptoms are rare with this disease: for about 95% of patients, the first symptom is often death (Elefteriades 2008). Rupture and dissection can be avoided through elective surgical repair; however, identifying individuals at risk is challenging. Currently, the clinical decision whether to electively repair an AsAA (Coady et al. 1997) is mainly based on the aortic size, where intervention is typically recommended if the maximum diameter of the ascending aorta exceeds 5.5 cm. This is supported by the positive correlation between the size and rupture or dissection (Coady et al. 1997). A relative aortic size index (ASI) normalized by the patient body surface area has also been used for clinical assessment of risk (Davies 2006).

However, the maximum aortic diameter may not accurately reflect an AsAA patient's risk (Elefteriades and Farkas 2010; Fillinger 2004; Nishimura et al. 2014): aneurysms at small diameter (e.g., 3.5 cm) have been known to rupture (Elefteriades and Farkas 2010). The impact of AsAA geo-

Published online: 06 April 2017

metric features, other than diameter, on patient risk has been investigated in several studies. Celi and Berti (2014) performed finite element analysis of TAA and showed that some morphological parameters (e.g., maximum diameter ratio, lesion extension ratio and eccentricity ratio) could significantly affect the wall stress, but did not provide any predictive model for risk assessment. There are many studies (Choke et al. 2005; Doyle et al. 2009; Georgakarakos et al. 2010; Raut et al. 2013; Rodríguez et al. 2008; Ryu et al. 2011) in which geometric features were used for risk analysis of abdominal aortic aneurysms (AAA). However, these studies only considered intuitive geometric parameters (Shum et al. 2011), such as asymmetry, aspect ratio, curvature, torsion and tortuosity, which may not fully describe the variations of AAA geometries.

To more rigorously describe the AsAA geometries, statistical shape modeling may be a better approach. Usually based on principal component analysis (PCA), a statistical shape model (SSM) represents the shape probability distribution by a mean shape and modes of shape variations where a shape is simply a vector composed of spatial point coordinates. SSMs have been extensively used in computer vision and biomedical image analysis applications for object detection, shape reconstruction and motion tracking (Cootes et al. 1995; Heimann and Meinzer 2009; Staib and Duncan 1996) where SSMs were used to model subtle variations in shape compared to the population mean. There are also a few applications of using SSM to study organ functional status. For instance, Wu et al. (2012) built a SSM of the human right ventricle for classification of hypertension.

Finite element (FE) analyses have been utilized for studying aortic aneurysm biomechanics and rupture risk (Celi and Berti 2014; Doyle et al. 2009; Erhart 2015; Fillinger et al. 2002; Gasser 2016; Georgakarakos et al. 2010; Maier et al. 2010; Martin et al. 2015; Rodríguez et al. 2008; Venkatasubramaniam 2004; Vorp et al. 1998). The main limitations in these studies are the use of simplified and isotropic tissue properties (Celi and Berti 2014; Doyle et al. 2009; Fillinger et al. 2002; Georgakarakos et al. 2010; Maier et al. 2010; Vorp et al. 1998), idealized geometries (Celi and Berti 2014; Rodríguez et al. 2008; Vorp et al. 1998), neglect of pre-stress (Celi and Berti 2014; Doyle et al. 2009; Georgakarakos et al. 2010) and lack of tissue failure criteria (Celi and Berti 2014; Doyle et al. 2009; Georgakarakos et al. 2010; Rodríguez et al. 2008). To obtain more accurate FE modeling of AsAA rupture, our group (Martin et al. 2015) utilized anisotropic hyperelastic material models and conducted biaxial tissue testing to obtain material parameters as reported in (Martin et al. 2013; Pham et al. 2013b). The results showed good agreement between FE simulations and clinical findings (Martin et al. 2015). However, our previous study showed the mixed effect of shape and material property; thus, it is not clear how shape variation alone can affect AsAA rupture risk.

Although FE analyses have great potential for clinical applications, it may take hours to set up and run a FE simulation of AsAA rupture, not to mention possible numerical convergence issues, preventing fast feedback to clinicians. Since machine learning techniques have been highly successful in many applications of computer-aided diagnosis (Doi 2008; Ginneken et al. 2011; Suzuki 2012), there may be a solution to this problem by using algorithms to learn the nonlinear relationship between the input (i.e., an AsAA shape) and the output (i.e., a risk metric) predicted by analyzing FE results. After the learning process, the risk score of an AsAA shape can then be given directly from the machine learning algorithms without any FE analysis.

In this study, we present a machine learning approach to establish the relationship between shape features and AsAA risk predicted by FE analysis, while keeping the other variables fixed by the following common simplifications on FE: one set of constitutive parameters, constant wall thickness and the same material strength. A SSM was built from a set of aorta shapes reconstructed from 3D CT images of 25 AsAA patients, for which the shapes were remeshed to build mesh correspondence. A total of 729 representative shapes were sampled from the shape distribution described by the SSM. The risk score of each shape was determined though FE analysis using our established approach (Martin et al. 2015), which was further enhanced with an improved backward displacement method for obtaining the unpressurized geometries. Support vector machine (SVM) and support vector regression (SVR) (Chang and Lin 2011; Cortes and Vapnik 1995) were used to determine the relationship between the risk and shape features, and cross-validation was performed to evaluate such relationship.

2 Methods

The overall study design is illustrated in Fig. 1. Briefly, given a set of aorta shapes reconstructed from 3D CT images, a SSM was built through a pipeline of remeshing, alignment and PCA, which is described in Sect. 2.1. A set of 729 shapes were sampled from the shape distribution. Pressure rupture risk is used as the risk metric, and the risk of each shape was obtained from FE analysis by estimating the unpressurized geometry and inflating each model to rupture, which is described in Sect. 2.2. Given the 729 sampled shapes with known rupture risk, classifiers and regressors based on different types of shape features were developed in order to predict a patient's rupture risk given the AsAA shape. The classifiers and regressors were trained and tested through tenfold cross-validation, which is described in Sect. 2.3.

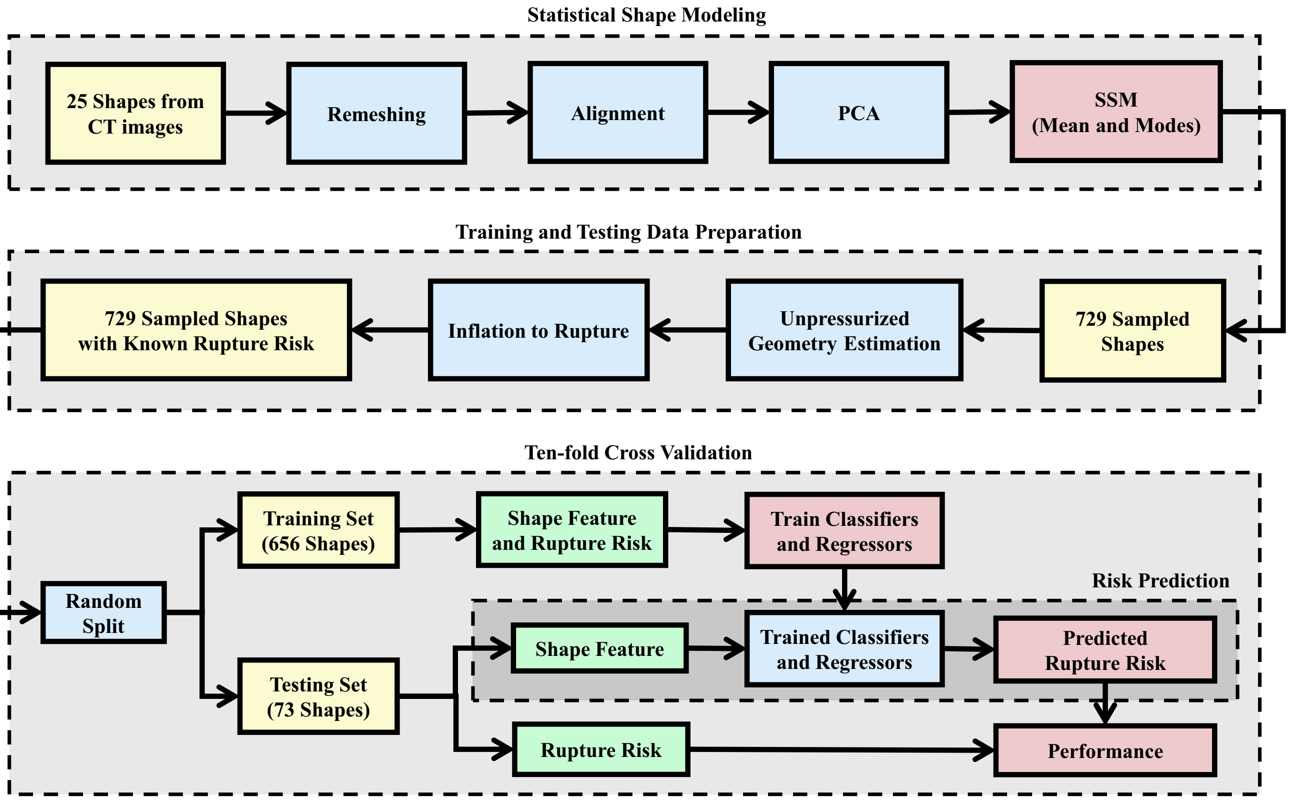

Fig. 1 Diagram of the modeling, simulation and evaluation process

2.1 Statistical shape modeling of the aorta

2.1.1 Image data

De-identified clinical cardiac CT scans and resected AsAA tissues were obtained for a total of 25 patients who underwent elective AsAA repair at Yale-New Haven Hospital between the years of 2008 and 2010 (Martin et al. 2015). Institutional review board approval to review de-identified images was obtained for this study. All patients underwent cardiac CT scans because of suspected AsAA prior to elective repair. The resolution of the images is 0.7 × 0.7 × 2.5 mm, and the field of view covers the thoracic and abdominal aorta. The AsAA tissue elastic and failure properties for the same patients were characterized from surgically resected tissues in a previous study (Martin et al. 2013).

As shown in Fig. 2, for each patient, the 3D surface of the aorta was semi-automatically reconstructed from the clinical CT image data using Avizo software (Burlington, MA). The surfaces were then trimmed at the ascending aorta just distal to the sinotubular junction on the proximal end and at the descending aorta on the distal end. The branch vessels at the arch were removed. The resulting surfaces were meshed to obtain a total of 25 aorta shapes in the form of triangle meshes with an arbitrary number of nodes and elements.

2.1.2 Aorta surface remeshing

To establish mesh correspondence between different patients and facilitate SSM and FE analyses, a remeshing method was developed in order to convert the triangle meshes to quad meshes with the same number of nodes and the same nodal connectivity among the elements for all patients. Briefly, as shown in Fig. 3, given a 3D triangle surface mesh as the input (Fig. 3a), a minimum-stretch-based mesh-parameterization was performed, resulting in a 2D triangle mesh in a rectangular shape of a predefined size (Fig. 3b). The 2D region was then discretized as a 2D quad mesh with 5100 nodes and 4950 elements (Fig. 3c). By using barycentric interpolation (Botsch et al. 2010) determined by the 3D surface mesh and the 2D triangle mesh, the 2D quad mesh was transformed into the 3D space and the nodes on the top and bottom of the rectangular mesh were merged together to yield a 3D tubular surface mesh with 5000 nodes and 4950 elements (Fig. 3d). Further details on the remeshing algorithms are provided in Appendix.

2.1.3 Shape alignment

After remeshing, each shape was aligned to a common coordinate system by Generalized Procrustes Analysis (GPA)

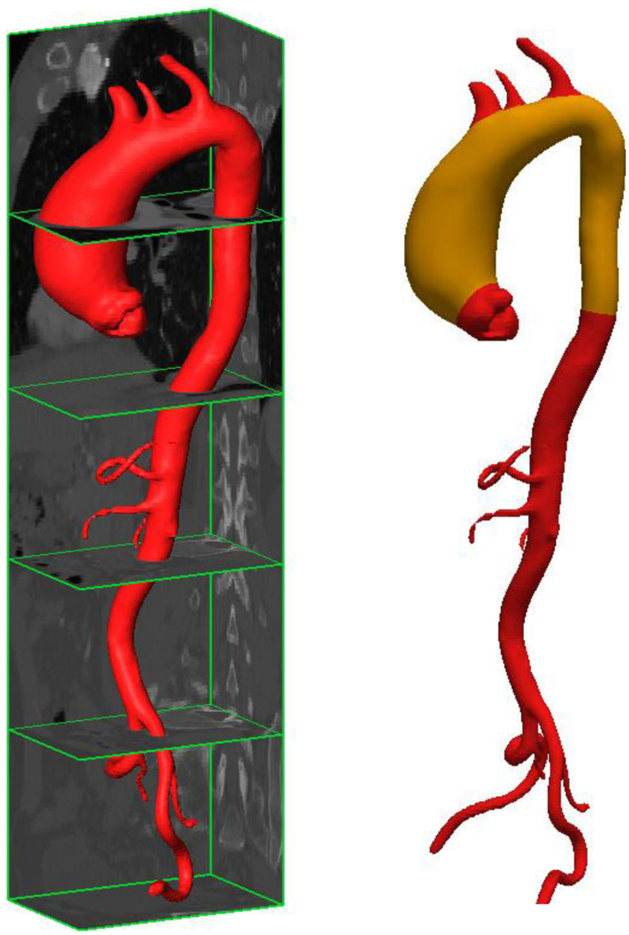

Fig. 2 **a** The aorta segmented from a 3D CT image. **b** Trimmed aorta surface in gold color

(Goodall 1991). Here, a shape $X^{(k)}$, indexed by k, is a quad-surface mesh which can be represented by a vector $X^{(k)} = [\boldsymbol{x}_1^{(k)}, \ldots \boldsymbol{x}_n^{(k)}, \ldots \boldsymbol{x}_N^{(k)}]$ assembled from the coordinates of each point $\boldsymbol{x}_n^{(k)}$ of the mesh with a total number of N points (i.e., nodes). The alignment process runs in an iterative manner: (1) transform each shape $X^{(k)}$ to the mean shape $\bar{X}$ by the similarity transform, where initially one of the training shapes is randomly chosen as the mean shape; (2) compute the mean shape from all the transformed shapes. The parameters of the similarity transform were determined by minimizing the objective function:

$$\min_{s,R,t} \sum_{k=1}^{K} \sum_{n=1}^{N} \|\bar{\boldsymbol{x}}_n - sR\boldsymbol{x}_n^{(k)} - \boldsymbol{t}\|^2, \quad (1)$$

where the mean shape is defined as $\bar{X} = [\bar{\boldsymbol{x}}_1, \ldots, \bar{\boldsymbol{x}}_n, \ldots, \bar{\boldsymbol{x}}_N] = \frac{1}{K}\sum_{k=1}^{K} X^{(k)}$, and $\bar{\boldsymbol{x}}_n$ is a point on the mean shape. K is the number of shapes. s is the scaling factor, R is the 3D-rotation matrix, and $\boldsymbol{t}$ is 3D-translation vector. The unknown parameters $\{s, R, \boldsymbol{t}\}$ of the similarity transform can be estimated by using a least-squares optimization method (Umeyama 1991). In this study, s was fixed as 1, and therefore, the scale information was retained.

2.1.4 Statistical shape model construction based on principal component analysis

Given the aligned shapes $\{X^{(1)}, ..., X^{(k)}, \ldots, X^{(K)}\}$ ($K = 25$), a SSM was built by PCA (Cootes et al. 1995; Heimann and Meinzer 2009). PCA can decompose the shapes into a mean shape and a set of linearly uncorrelated shape variations which are the principal components, also called the modes of shape variations. Standard PCA starts from assembling the covariance matrix C, given by

$$C = \frac{1}{K}\sum_{k=1}^{K}\left(X^{(k)} - \bar{X}\right)\left(X^{(k)} - \bar{X}\right)'. \quad (2)$$

Then, the eigenvalues and eigenvectors of the covariance matrix can be calculated. For this application, the number of points on each shape, $N = 5000$, is much larger than K and the rank of the matrix C is K. Singular value decomposition was applied to obtain a subset of the eigenvalues and eigenvectors, and the other eigenvalues are all zeros. The SSM was constructed with the mean shape $\bar{X}$ and the modes of shape variation $\left\{V^{(1)}, \ldots, V^{(K)}\right\}$ and the corresponding eigenvalues $\left\{\lambda^{(1)}, \ldots, \lambda^{(K)}\right\}$ which were sorted from largest to smallest.

2.1.5 Shape decomposition and shape sampling

By using the SSM, a shape Y can be decomposed into (i.e., approximated by) the mean shape plus a linear combination of the modes (i.e., shape variation), given by

$$Y \cong \bar{X} + \sum_{m=1}^{M} c_m \sqrt{\lambda^{(m)}} V^{(m)}. \quad (3)$$

Here, the shape Y has been aligned to the mean shape $\bar{X}$, and M is the number of selected modes.

A shape Y can be sampled from the shape distribution, Eq. (3), using a set of SSM parameters $\{c_1, ..., c_m, \ldots, c_M\}$. A large number of sampled shapes can represent the shape distribution and are more versatile than the original 25 shapes used in the SSM construction. In order to obtain a set of representative shapes, the selected modes must be able to explain a large percentage of the total shape variation, defined by

$$\frac{\text{Explained Variation}}{\text{Total Variation}} = \frac{\sum_{m=1}^{M}\lambda^{(m)}}{\sum_{k=1}^{K}\lambda^{(k)}}. \quad (4)$$

Fig. 3 Aorta surface quad-remeshing process. **a** Input 3D triangle mesh. **b** 2D triangle mesh, i.e., parameterization of **a**. **c** 2D quad mesh. **d** Output 3D quad mesh

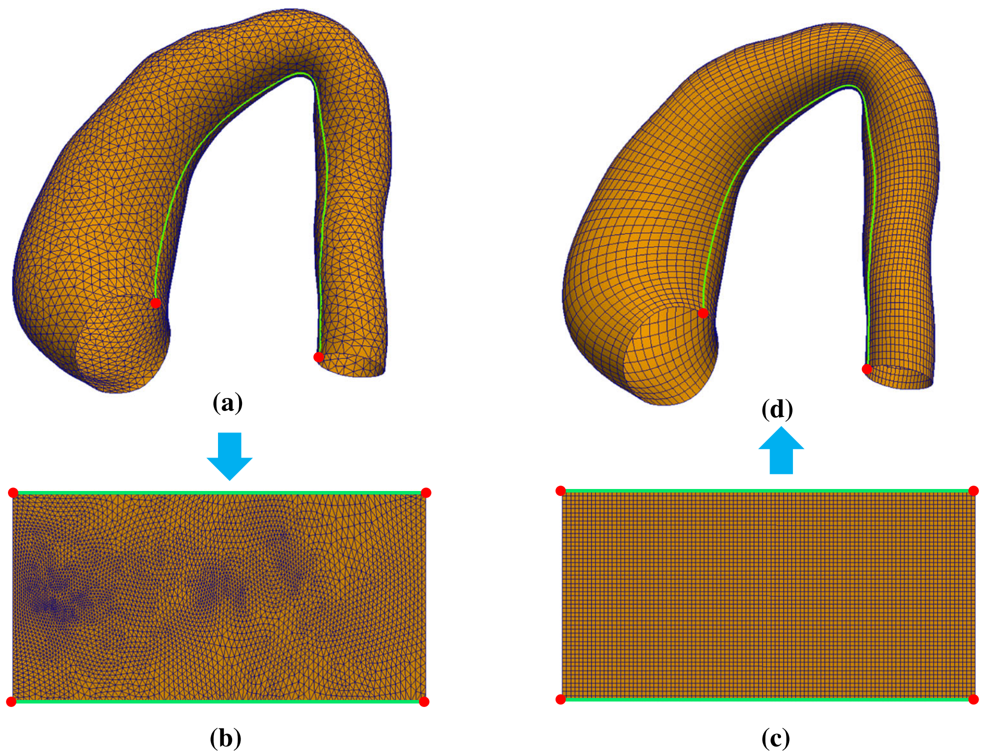

In this study, the first three modes were selected ($M = 3$) which explains 80.1% of the total shape variation. A total number of 729 shapes were obtained automatically by uniformly sampling the parameters $\{c_1, c_2, c_3\}$ in the range of -2 to 2, i.e., within 2 standard deviations of the mean shape.

2.2 Finite element modeling of AsAA

Finite element (FE) analyses were performed on the 729 AsAA shapes which were prescribed AsAA tissue properties determined previously (Martin et al. 2013) using ABAQUS/Standard 6.14 (Simulia, RI). FE analyses consisted of two steps: (1) backward displacement method to estimate the unpressurized AsAA geometry and (2) inflation of the unpressurized geometry to rupture. S4R shell elements were used during step 1, and to improve convergence S4 shell elements were used during step 2. The AsAA wall was prescribed a uniform thickness of 2 mm (Martin et al. 2015) at the unpressurized state, which is the mean thickness based on our experimental data (Pham et al. 2013a). While assumed thickness is a limitation, it is currently not possible to measure wall thickness from CT images due to the partial volume effect (Barrett and Keat 2004). In all simulations, pressures were applied uniformly to the inner surface of the aorta models, and the boundary nodes of the aorta models, i.e., the proximal and distal ends of the model, were only allowed to move in the radial direction based on the local coordinate system. The FE simulations of all the shapes were run automatically via a custom MATLAB (Mathworks, MA) program.

2.2.1 Constitutive modeling of AsAA tissue

A fiber-reinforced hyperelastic material model based on the work of Gasser et al. (2006) was used to characterize the mechanical response of AsAA tissue. The tissues were hereby assumed to be composed of a matrix material with two families of embedded fibers, each with a preferred direction. The strain energy function can be expressed as

$$W = C_{10}\left\{\exp\left[C_{01}\left(\bar{\boldsymbol{I}}_1 - 3\right)\right] - 1\right\} + \frac{k_1}{2k_2}\sum_{i=1}^{2}\left[\exp\left\{k_2[\kappa\bar{\boldsymbol{I}}_1 + (1-3\kappa)\,\bar{\boldsymbol{I}}_{4i} - 1]^2\right\} - 1\right], \tag{5}$$

where C_{10} and C_{01} are material constants to describe the matrix material, k_1 and k_2 are material constants used to describe the fiber material, $\bar{\boldsymbol{I}}_1$ is the first strain invariant, and $\bar{\boldsymbol{I}}_{4i}$ is equal to the square of the stretch in the fiber direction, i. The fiber orientation was defined by $\boldsymbol{M}_i = \boldsymbol{m}_{0_i} \otimes \boldsymbol{m}_{0_i}$ with $\boldsymbol{m}_{0_1} = [\cos\theta, \sin\theta, 0]$ and $\boldsymbol{m}_{0_2} = [\cos\theta, -\sin\theta, 0]$, where the mean fiber orientation in the local coordinate system is described by θ, and κ is a dispersion parameter describing the distribution of the fiber orientation.

As the interest of this study lies in the geometric effect on AsAA rupture risk, the material property of the AsAA tissue was fixed for all the simulations. The material model was fitted to the seven protocol biaxial testing data of an AsAA tissue sample from a patient, representing the approximate

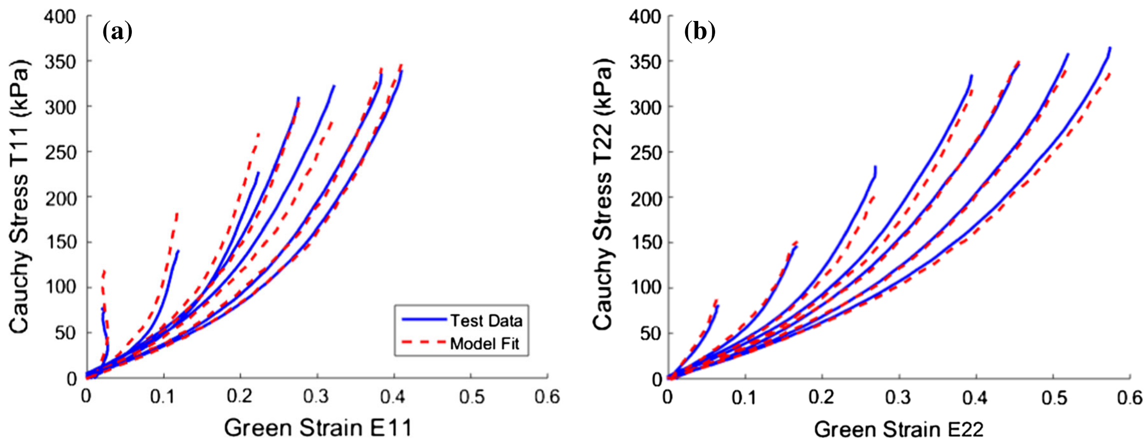

C_{01}	C_{10} (kPa)	k_1 (kPa)	k_2	κ	θ (°)	R^2
1.66	20.68	5.79	2.24	0.16	0.18	0.9873

Fig. 4 Seven protocol biaxial response and model fit in the **a** circumferential and **b** axial directions. (*table*) Fitted model parameters. The goodness of fit is R^2. T11 is in circumferential direction, and T22 is in axial direction

mean AsAA tissue response (Fig. 4) among the tested samples from the patients (Martin et al. 2015).

The equivalent strain from the tissue damage theory (Simo 1987) was used to define the failure properties of the AsAA tissue, by the expression

$$\Xi_s = \sqrt{2\mathrm{W}}. \tag{6}$$

where W is the strain energy calculated by using Eq. (5). Tissue failure was considered to occur when $\Xi_s \geq \Xi_f$, where Ξ_f is the failure equivalent strain. The mean Ξ_f of $18.34(kPa)^{1/2}$ determined through experimental tests on AsAA tissue from a previous study (Martin et al. 2015) was used as the failure criterion. Equations 5 and 6 were implemented in ABAQUS via a user-material subroutine. In this study, we use the failure equivalent strain as the rupture criterion, and the dynamic process of tissue rupture is not modeled.

2.2.2 Improved backward displacement method for unpressurized geometry estimation

As the AsAA shapes were obtained at in vivo configuration from CT scans under systolic pressure (120 mmHg), directly applying the physiological loading pressure to these shapes would result in inaccurate calculations of the stress and strain fields in FE analysis. Thus, the unpressurized geometry of each shape was recaptured and used for FE analysis. Here, the backward displacement method (Bols et al. 2013) was utilized and further improved upon to restore the unpressurized geometry.

The improved backward displacement method is illustrated in Fig. 5. In iteration i, the unpressurized geometry estimation $Y_0(i-1)$ from the previous iteration is updated by adding a scaled difference between the pressurized geometry $Y_{sysFE}(i-1)$ and the in vivo geometry Y_{img} at the systole phase. The method can be expressed as

$$Y_0\,(i) = Y_0(i-1) + \alpha[Y_{img} - Y_{sysFE}(i-1)]. \tag{7}$$

Here, $Y_0(i)$, Y_{img} and $Y_{sysFE}(i)$ are vectors assembled from all the nodal coordinates. The scaling factor α is in the range of 0 to 1. The initial unpressurized geometry $Y_0(1)$ was set to the in vivo configuration geometry Y_{img}.

In the backward displacement method proposed by Bols et al. (2013), there is no scaling factor, i.e., α is always 1, and the in vivo pressure load is used throughout the iterations. This method resulted in FE convergence issues for our application: FE simulations break down due to the large changes in model shape from one iteration to the next. We found that a small α may prevent this problem; however, as α gets smaller, more iterations are needed to achieve a converged solution for Eq. 7. In this study, α was set to 0.5 which is approximately equal to the ratio between the size of an unpressurized geometry and the size of the corresponding in vivo geometry, and the maximum number of iterations was set to 10. In addition to ensure FE convergence, only half of the systolic pressure (60 mmHg) was applied at the first iteration, and from the second iteration, full pressure (120 mmHg) was applied. With these improvements, all of the FE simulations converged, and all of the unpressurized geometries were obtained.

2.2.3 Inflation of AsAA until reaching the rupture criterion

Once an unpressurized geometry was obtained by using the improved backward displacement method, incremental pres-

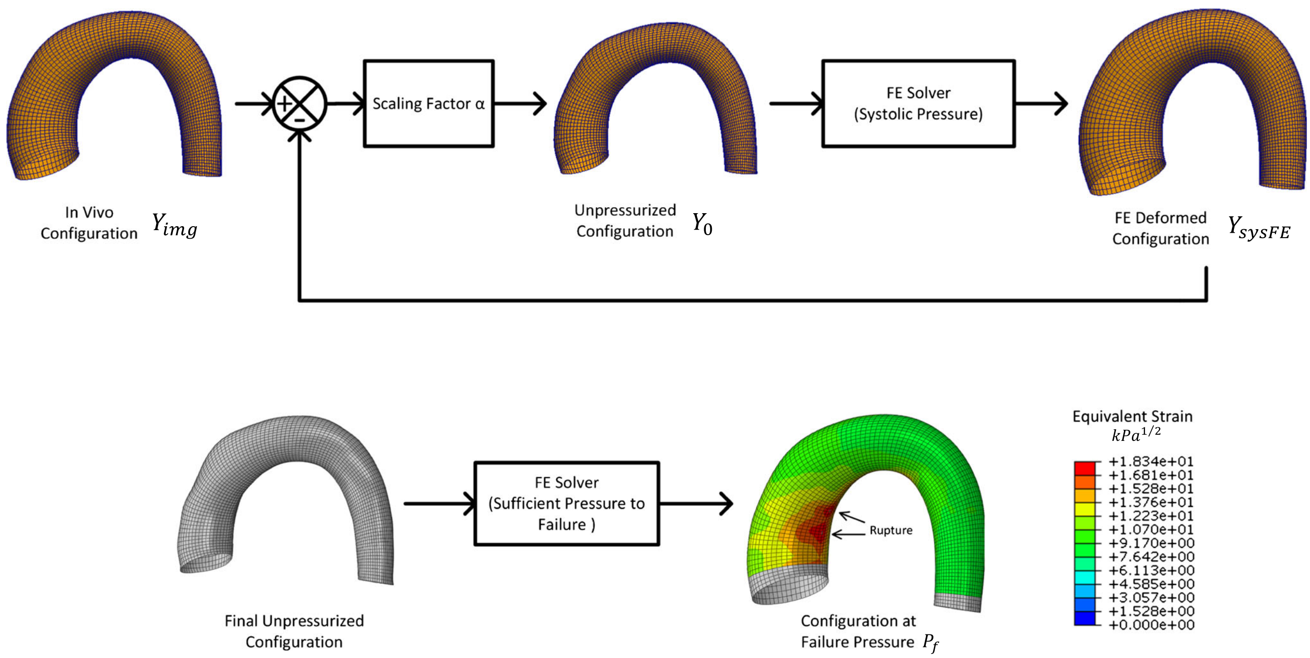

Fig. 5 Diagram of the improved backward displacement method and inflation to rupture

sure was applied to the unpressurized geometry until the rupture criterion is reached in Sect. 2.2.1. Once the criterion is reached, an AsAA is considered as ruptured. Equivalent strain values at 4 layers of elements adjacent to the mesh boundaries were excluded in the analysis in order to avoid boundary effects. The failure pressure P_f was extracted from the FE analyses at the time increment immediately preceding tissue failure (i.e., when $\Xi_s = \Xi_f$). The pressure risk ratio (PRR), P_{sys}/P_f, as defined previously (Martin et al. 2013) was used as a measure of rupture risk. P_f varies with different shapes, and P_{sys} is the constant systolic pressure (120 mmHg). PRR ranges from 0 to 1 where a higher value indicates a higher risk of rupture. Patients with P_f lower than, or equal to, 160 mmHg, representing the hypertension stage 2 pressure level, were considered to be at high rupture risk, which translates to a PRR higher than, or equal to, 0.75. Patients with P_f higher than 160 mmHg were assumed to have low rupture risk, corresponding to a PRR below 0.75.

2.3 Machine learning-based rupture risk analysis using FE simulation results

2.3.1 Shape features

For each shape at the systolic phase, four types of shape features were obtained: (1) maximum diameter, (2) the average curvature of the centerline, (3) the average curvature of the surface, and (4) the SSM parameters $[c_1, c_2, c_3]$. Since a quad-surface mesh is topologically equivalent to a rectangular grid, the surface consists of closed circumferential curves, i.e., a set of rings along the centerline. For each curve, the average position of the points on the curve is calculated, and the mean distance between the average position and each point on the curve is also calculated as the radius of the curve. The centerline is assembled from those average positions, and its average curvature is calculated. The maximum diameter is just the maximum value of the diameters of the curves. The surface curvature at each node is quantified as the mean curvature (Botsch et al. 2010), and then the average curvature is calculated. The SSM parameters can be obtained from the statistical shape model by Eq. (3).

2.3.2 Classification

Based on the FE simulation results, the 729 sampled shapes were divided into low and high risk groups as described in Sect. 2.2.3. Given this dataset consisting of the two groups, classifiers were built to take the feature of a shape as the input and predict the group index of the shape, i.e., low risk or high risk. For this study, support vector machine (SVM) classifiers (Chang and Lin 2011; Cortes and Vapnik 1995) were used with radial basis kernel. To evaluate the performance of a classifier, tenfold cross-validation was applied: all the data were randomly partitioned into ten subsets, then one subset was used as the testing set to evaluate the performance of the classifier, and the others were used as the training set to find the optimal parameters of the classifier. This process was repeated 100 times to obtain mean and

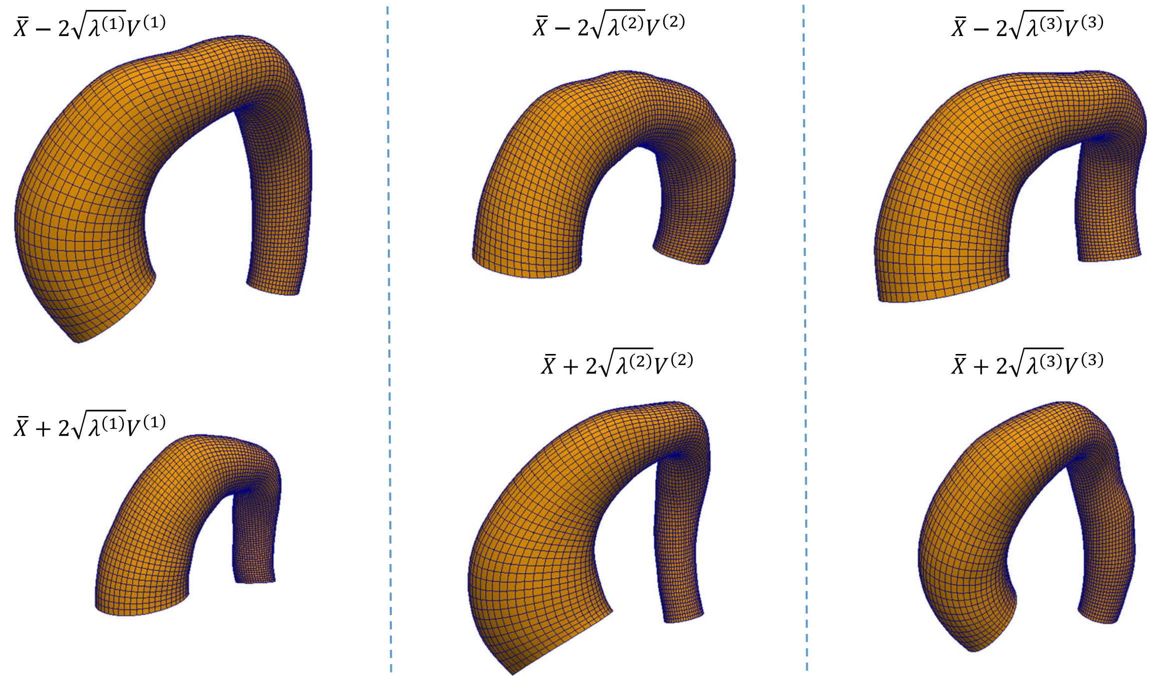

Fig. 6 Examples of the first three modes of shape variation. The mean shape is shown in Fig. 5

standard deviation of the performance scores (accuracy, sensitivity and specificity) on the testing sets. Accuracy was defined as (TP + TN)/(TP + TN + FP + FN), sensitivity was defined as TP/(TP + FN), and specificity was defined as TN/(TN + FP), where true positive (TP) is the number of high risk shapes correctly identified as high risk; false negative (FN) is the number of high risk shapes incorrectly identified as low risk; true negative (TN) is the number of low risk shapes correctly identified as low risk; and false positive (FP) is the number of low risk shapes incorrectly identified as high risk.

2.3.3 Regression

The classifiers can only make a binary decision about the rupture risk of a shape. It would be more valuable if the PRR value could be directly inferred from each shape. Thus, regression methods were used to map shape features directly to PRR. Three types of regression methods were tested, linear regression, logistic regression and support vector regression (SVR). SVR (Chang and Lin 2011; Vapnik 1998) is a variant of SVM and can describe the nonlinear relationships between shape features and PRR. The root-mean-square error (RMSE) was used to measure regression accuracy. To evaluate the performance of each regressor, tenfold cross-validation was applied, similar to the performance evaluation procedure for classification. The mean and standard deviation of the RMSE values on the testing sets were calculated from cross-validation.

3 Results

3.1 Statistical shape modeling

As shown in Fig. 6, the first mode of shape variation mainly describes the overall changes in size. The second and the third modes mainly describe the diameter variations along the centerline and the variations in centerline curvature and surface curvature.

3.2 Finite element simulation of AsAA inflation

Using the improved backward displacement method, the unpressurized geometries of all the sampled shapes (729 shapes) were obtained with an accuracy of approximately 1% within 10 iterations. It took about 30 min on average to estimate an unpressurized geometry on a PC with a 3.6-GHz quad core CPU and 32-GB RAM. The node-to-node mean distance error was calculated for each pair of pressurized geometry, $Y_{sysFE}(i)$, and systolic geometry, Y_{img}, at each iteration i, and normalized by the maximum radius of Y_{img}. The mean and standard deviation of the normalized distance errors calculated at each iteration across all the shapes are shown in Fig. 7.

AsAA inflation was simulated from the unpressurized geometries, and the PRR was obtained for all the shapes. The results are visualized in Fig. 8, where a subset of the shapes are color-coded with their pressure risk ratios and arranged

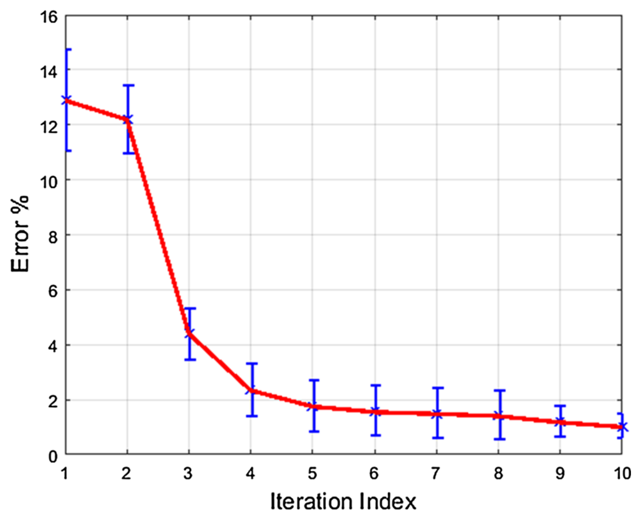

Fig. 7 Mean and standard deviation of the normalized distance errors at each iteration

in the SSM parameter space. Note that several large shapes had low PRR, while several small shapes had high PRR.

3.3 Classification-based rupture risk analysis

SVM classifiers were built and tested for different shape features to identify shapes with low or high rupture risks. The performance of the classifiers on the testing sets from tenfold cross-validation is reported in Table 1. The classification performance of the individual intuitive shape features, i.e., diameter, curvature, was fairly low. When each of these features was combined, the classification performance was improved; however, it was still inferior to that of the SSM parameters.

For the purpose of visualization of the results in Table 1, we applied two of the classifiers to the whole dataset and drew the decision boundaries (line or surface), which are shown in Fig. 9. It can be clearly seen that the surface generated by SVM using the SSM parameters can delineate the low and high risk shapes more accurately.

Rule-based classification of rupture risk: To mimic the diameter-based clinical decision rule on electively repair (Coady et al. 1997; Davies et al. 2002), a rule-based classifier was tested, where a shape is deemed high risk if the maximum diameter is larger than 5.5 cm. This classifier had an accuracy of 53.1%, a sensitivity of 7.8% and a specificity of 100% on the whole dataset of the 729 sampled shapes.

3.4 Regression-based rupture risk analysis

Linear regression, logistic regression and support vector regression were performed to find the relation between shape features and PRR. The performance of the regressors (RMSE

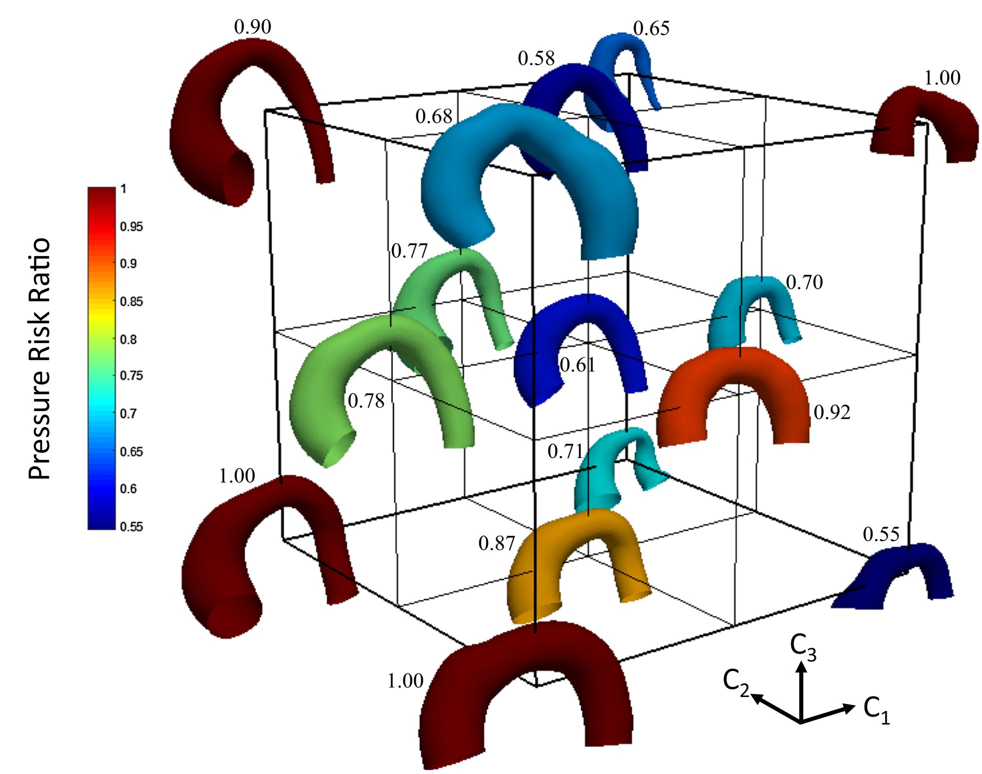

Fig. 8 Shapes color-coded with pressure risk ratios and arranged in SSM parameter space

Table 1 Classification performance

Feature	Accuracy (%)	Sensitivity (%)	Specificity (%)
Maximum diameter	69.86 ± 5.28	68.69 ± 7.25	71.19 ± 7.97
Centerline curvature	58.78 ± 5.32	69.40 ± 8.14	48.37 ± 7.29
Surface curvature	69.71 ± 5.11	76.29 ± 6.55	63.23 ± 7.62
All above features	87.01 ± 3.96	86.04 ± 5.22	87.96 ± 5.83
SSM parameter $[c_1, c_2, c_3]$	95.58 ± 1.89	95.64 ± 3.27	95.55 ± 3.00

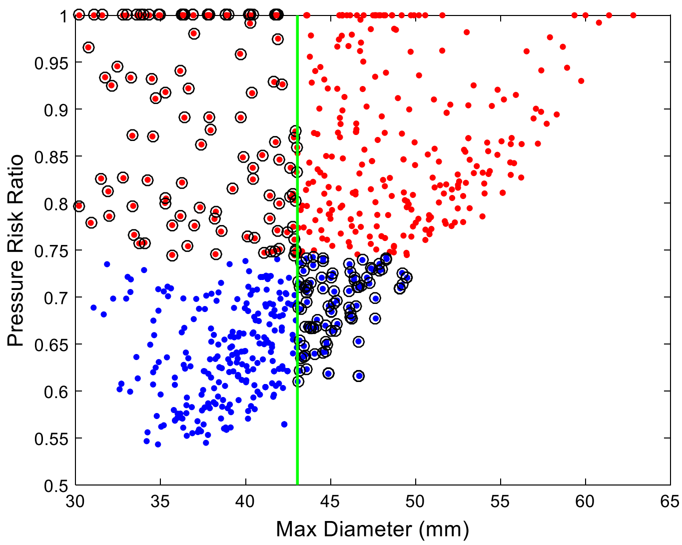

(a)

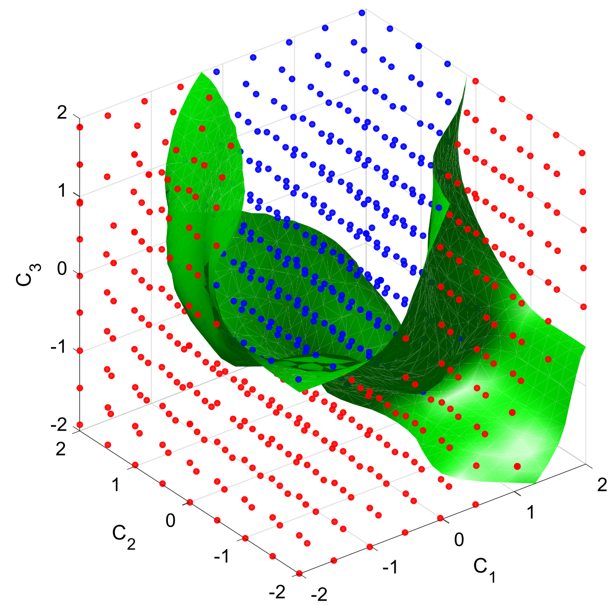

(b)

Fig. 9 **a** Classification result using max diameter as the shape feature. *Blue dots* indicate shapes in the low risk group. *Red dots* indicate *shapes* in the high risk group. *Dark circles* indicate misclassified shapes. The *green line* is the decision boundary (max diameter at 43.05 mm). **b** Classification result using the SSM parameters as the shape feature. *Blue* and *red dots* indicate low and high risk shapes, respectively. The *green* surface is the decision boundary

values) on the testing sets from tenfold cross-validation is listed in Table 2. The RMSE was similar for all of the shape features using linear and logistic regression methods. The RMSE was lowered using SVR with a combination of the intuitive shape features and was further reduced by approximately 50% using SVR with the SSM parameters.

For the purpose of visualization of the results in Table 2, two of the regressors were applied to the whole dataset. The regression results (line or isosurfaces) are plotted with the PRR data and prediction errors in Fig. 10. The magnitude of prediction errors of the diameter-based regressor was large, particularly for higher PRRs where the prediction errors became increasingly negative, indicating that the diameter regressor may underestimate high PRR. The prediction errors for the SSM parameter-based regressor were much smaller and more uniformly distributed.

4 Discussion

This study lies in the broad field of computer-aided diagnosis (Doi 2008; Ginneken et al. 2011; Suzuki 2012) in which computer algorithms are developed to assist clinicians in decision making. We proposed a novel approach combining FE analysis and machine learning techniques including SSM, SVM and SVR, to study the relationship between shape features and a risk metric of AsAA. To our best knowledge, it is the first time that these machine learning techniques are used to establish the nonlinear relationship between shape features and aneurysm risk predicted by FE analysis. We also developed algorithms for quad-surface remeshing and improved the backward displacement algorithm for recovering unpressurized geometries.

Training data are essential for machine learning. In this study, only 25 sets of patient image data were used; however, by using the SSM to sample the shape distribution,

Table 2 Regression performance (RMSE)

Feature	Support vector regression	Logistic regression	Linear regression
Maximum diameter	0.1270 ± 0.0125	0.1245 ± 0.0095	0.1234 ± 0.0093
Centerline curvature	0.1325 ± 0.0110	0.1303 ± 0.0087	0.1301 ± 0.0087
Surface curvature	0.1196 ± 0.0105	0.1192 ± 0.0090	0.1181 ± 0.0092
All above features	0.0686 ± 0.0074	0.1164 ± 0.0089	0.1152 ± 0.0089
SSM parameter $[c_1, c_2, c_3]$	0.0332 ± 0.0035	0.1143 ± 0.0085	0.1120 ± 0.0088

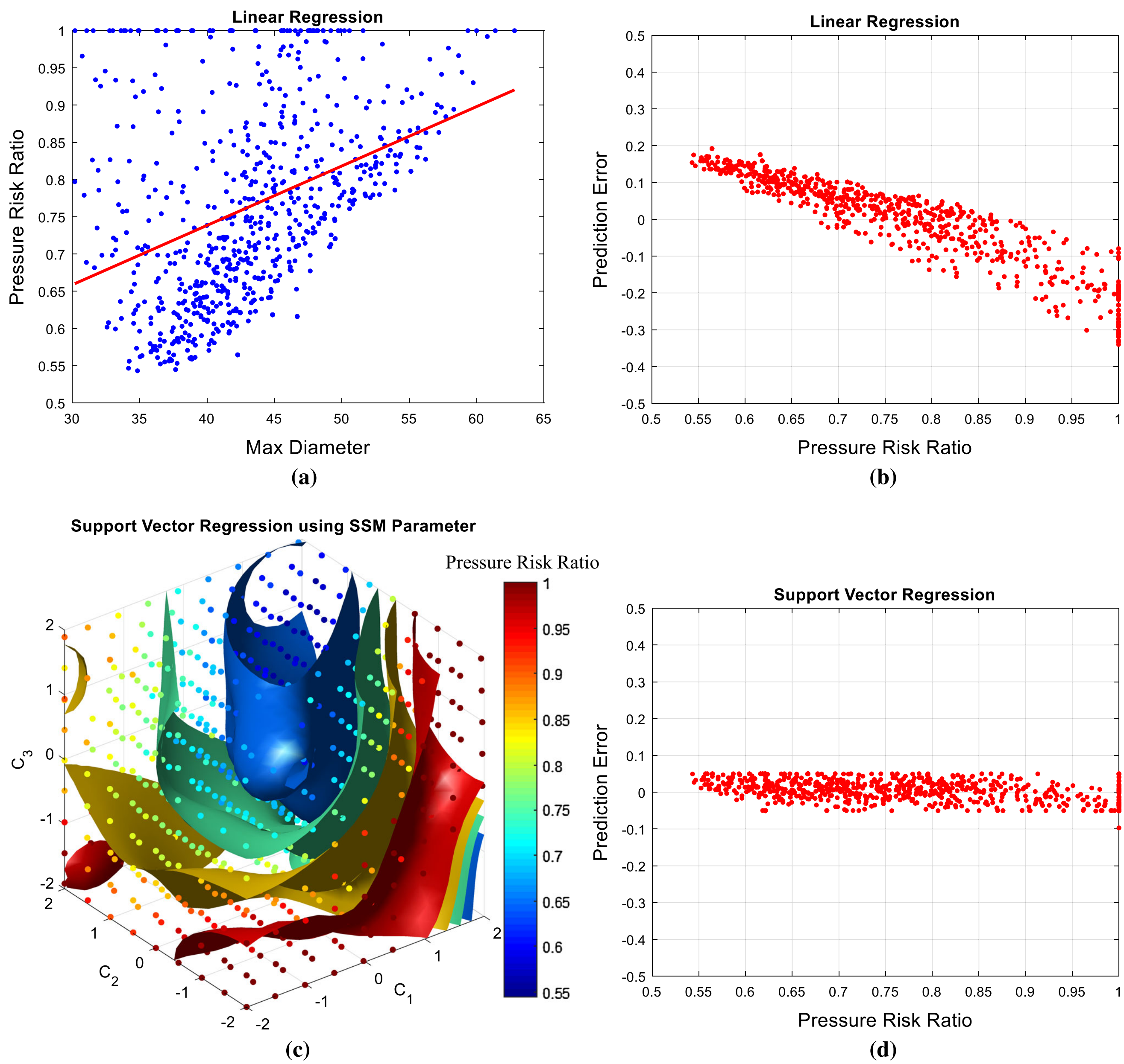

Fig. 10 **a** Linear regression using max diameter as shape feature where the *red line* is the regression line and **b** the associated prediction errors versus PRR. **c** Support vector regression using the SSM parameters as shape feature, where each color-coded surface corresponds to a predicted PRR, i.e., isosurface of PRR, and **d** the associated prediction errors versus PRR

729 shapes were obtained for algorithm training and testing. Those shapes could be considered as belonging to 729 virtual patients. A nice property of the SSM developed in this study is that it was constructed with quad elements by using the surface remeshing algorithms, which are preferred over triangular elements for FE analysis, and it is known that quad mesh generation is a challenging task (Alliez et al. 2008; Bommes et al. 2013; Botsch et al. 2010). The surface remeshing algorithms can be used for other FE applications. The risk of each shape was predicted by FE analysis, and the FE models incorporated average AsAA tissue thickness, mean elastic response and failure properties derived from experiments (Martin et al. 2015, 2013; Pham et al. 2013a) and accurately estimated unpressurized geometries by using the improved backward displacement method. The improved backward displacement approach can potentially be used for other applications and is simple to implement compared to alternative methods (Gee et al. 2010; Lu et al. 2007; Raghavan et al. 2006; Weisbecker et al. 2014).

The FEA results for 729 shapes coincide with the clinical findings that rupture risk is high when the aortic diameter is larger than 5.5 cm, yet a small diameter does not necessarily mean low rupture risk. Therefore, the 5.5-cm-diameter rule for surgical intervention may not be sensitive enough to identify patients at high risk with small AsAA size. Machine learning algorithms were trained on the shape features and FEA results. The accuracy of the machine learning algorithms to predict AsAA rupture risk was dependent on the type of shape features. Using the SSM parameters as the shape features has led to a much higher accuracy for classification and regression than the intuitive geometric features, even when a combination of these features was used. These observations are in line with the results in (Hua and Mower 2001) which also showed that simple geometric characteristics cannot reliably predict AAA wall stresses. Interestingly, while using the SSM parameters, small AsAAs (low c_1) associated with high risk were also identified (Fig. 8). The SVM classification and SVR regression accuracy obtained with the SSM parameters in this study, i.e., SVM classification accuracy of 95.58% and SVR regression error of 0.0332, demonstrate that the machine learning approach may replace FE analysis by learning the nonlinear relationship between the input and the output of FE analysis.

As more patient data are collected, more modes of shape variation can be included in the SSM to further improve the classification and regression accuracy. The benefit of this approach is that for an input AsAA shape, it only takes a few seconds for SVM or SVR to produce the output, which is magnitudes faster than FE simulation and eliminates numerical convergence issues associated with FEA. By using the image segmentation method (Liang et al. 2016) we recently developed, the time for geometry reconstruction will be reduced to a few minutes.

Limitation and future work

Since the goal of this study was to evaluate shape features as risk predictors, we kept the other variables fixed while varying the shape, which is similar to related approaches in the literature (Celi and Berti 2014; Choke et al. 2005; Doyle et al. 2009; Fillinger et al. 2002; Georgakarakos et al. 2010; Raut et al. 2013) that mainly studied the effect of intuitive geometric features on the prediction of wall stress by keeping material parameters and wall thickness fixed. Therefore, this study has the following limitations: (1) one set of constitutive parameters which represents only the mean response, (2) the mean material strength (i.e., failure threshold), (3) a mean thickness, (4) removal of branching vessels at the arch and (5) neglect of residual stress. While (5) is very challenging to resolve, it is possible to incorporate the factors (1–4) into the machine learning approach in our future work.

It is straightforward to include the branching vessels in the mesh model by applying the remeshing algorithms to the surface of the branching vessels and stitching all the mesh segments together. It is also possible to obtain the heterogeneous thickness of the aortic wall in vivo by using advanced MR imaging (Dieleman et al. 2014). To use thickness information as a risk indictor, similar to the SSM model, a statistical thickness model (STM) can be built from training data, for which PCA can be used to describe the variations of thickness. Thus, STM parameters will be combined together with SSM parameters as risk indictors.

To incorporate information about material elastic property, the geometries at two cardiac phases can be used. Based on the study in Wittek et al. (2013, 2016), the parameters of a given constitutive model can be identified from the aorta shapes at two cardiac phases with known blood pressure level (e.g., systole and diastole), which implies material elastic property information is contained in the two geometries. Thus, we will build two SSM models corresponding to the two cardiac phases, representing the joint distribution of shape and material elastic property.

The threshold of tissue failure (i.e., material strength) can vary among different patients, and modeling of material strength is a very challenging task. We will try to use statistical methods (Pham et al. 2013a; Vande Geest et al. 2006) to build the probability distributions of material strength in age/gender/genetic groups, and these distribution models can be used to perform a sensitivity analysis, i.e., providing a mean and standard deviation of risk for each patient. In the machine learning approach, instead of just learning a scalar risk, the mean and standard deviation will both be learned, i.e., learning the statistical relationship instead of the deterministic one.

5 Conclusion

In this study, we proposed a machine learning approach to establish the relationship between shape features and AsAA risk predicted from FE analysis. CT image data for 25 AsAA patients were used for building a SSM of the AsAA to describe the distribution of shapes across the population, for which quad-surface remeshing was preformed to maintain mesh correspondence between different shapes. A total of 729 shapes were sampled from the shape distribution and utilized in FE analyses to determine the risk of each shape. SVM classifiers and SVR regressors using different shape features were trained with the FE analysis results to determine the relationship between shape features and the risk. Using the SSM parameters as the shape feature, SVM classification achieved an accuracy of 95.58%, and SVR regression achieved an error of 0.0332, which indicates that SVM and SVR coincide with FE analysis and SSM parameters are strong shape features. This approach may also serve as a faster surrogate for FEA. In future work, we will incorporate material properties and inhomogeneous thickness in the machine learning approach to build a practical system for noninvasive AsAA risk assessment.

Acknowledgements Research for this project was funded in part by NIH Grant R01 HL104080. Liang Liang is supported by an American Heart Association Post-doctoral Fellowship 16POST30210003.

Compliance with ethical standards

Conflict of interest An Intellectual Property Disclosure has been filed on the techniques and procedures at Georgia Tech Research Corporation.

Appendix

The surface remeshing method has three steps:

Step-1: Find the shortest path between a node on the left boundary and a node on the right boundary. Given a pair of nodes on the left and right boundaries, the geodesic path between them is recovered. The points on the geodesic path are on the 3D surface, but may not be the nodes of the mesh. Then a set of geodesic paths are obtained for every pair of boundary nodes, and the shortest path is selected as a cut-line. The surface mesh is cut open along the cut-line as shown in Fig. 3a, and it becomes topologically equivalent to a rectangle.

Step-2: Compute mesh-parameterization of the 3D surface mesh. The 3D surface mesh, which is cut along the cut-line, is mapped onto a 2D rectangular region, which is called mesh-parameterization. After the mapping, the 3D surface mesh is transformed to a 2D planar triangle mesh as shown in Fig. 3b.

Step-3: Divide the 2D rectangular region into a 2D quad mesh and transform it to 3D. The 2D rectangular region is discretized into a 2D mesh with rectangular elements (i.e., quad elements), as shown in Fig. 3c. Then the transform from the points of the 2D quad mesh to the 3D surface is determined by barycentric interpolation (Botsch et al. 2010) of the 2D triangle mesh. After transforming the 2D quad mesh to the 3D surface and sealing the transformed mesh along the cut-line, a 3D surface mesh with quad elements is obtained, as shown in Fig. 3d.

We utilized the exact geodesic path finding algorithm proposed by Surazhsky et al. (2005), for *Step-1*. Based on the work of Yoshizawa et al. (2004), we developed a stretch-minimizing-based algorithm for *Step-2*, and it has two stages:

Stage-1 of Step-2: Find an initialization mesh-parameterization based on barycentric mapping and mean value theorem (Botsch et al. 2010). Barycentric mapping is used to build a parameterization of the 3D triangle surface mesh, i.e., transforming the 3D surface mesh to a 2D planar triangle mesh. The boundary of the 2D planar mesh forms a rectangle. Each triangle $\boldsymbol{P}_i = (\boldsymbol{p}_1, \boldsymbol{p}_2, \boldsymbol{p}_3)$ of the 3D surface mesh is mapped to a triangle $\boldsymbol{Q}_i = (\boldsymbol{q}_1, \boldsymbol{q}_2, \boldsymbol{q}_3)$ of the 2D planar mesh. Each node $\boldsymbol{p}_i = [x_i, y_i, z_i]$ of the 3D surface mesh is mapped to a node $\boldsymbol{q}_i = [u_i, v_i]$ of the 2D planar mesh. Here $[x_i, y_i, z_i]$ denotes 3D coordinate, and $[u_i, v_i]$ denotes 2D coordinate. Based on barycentric mapping, the node coordinates of the 2D planar mesh are determined by

$$\begin{cases} \sum_{j=1}^{M} a_{i,j} u_j = -\sum_{j=M+1}^{N} a_{i,j} u_j \\ \sum_{j=1}^{M} a_{i,j} v_j = -\sum_{j=M+1}^{N} a_{i,j} v_j \end{cases} \tag{8}$$

where M is the number of interior nodes and N is the total number of nodes. By using the mean value theorem, each coefficient is determined by

$$a_{i,j} = \frac{1}{\|\boldsymbol{p}_i - \boldsymbol{p}_j\|} \left(\tan\left(\frac{\theta_{i,j}}{2}\right) + \tan\left(\frac{\delta_{i,j}}{2}\right) \right) \tag{9}$$

where $a_{i,j} > 0$ if $\boldsymbol{p}_i$ and $\boldsymbol{p}_j$ are connected by an edge, otherwise $a_{i,i} = -\sum_{j \neq i} a_{i,j}$ and $a_{i,j} = 0$. $\theta_{i,j}$ and $\delta_{i,j}$ are angles between the edge from $\boldsymbol{p}_i$ to $\boldsymbol{p}_j$ and its two adjacent edges, respectively. After the coefficients $\{a_{i,j}\}$ are calculated, the node coordinates of the 2D planar mesh are obtained by solving Eq. (1).

Now, an inverse transform from a point on the 2D plane to the 3D surface can be obtained: let $\boldsymbol{q}$ be a point inside $\boldsymbol{Q}_i$; then, its corresponding point $\boldsymbol{p}$ on the 3D surface is determined by an affine mapping, namely barycentric interpolation:

$$p = (\langle q, q_2, q_3 \rangle p_1 + \langle q, q_3, q_1 \rangle p_2 + \langle q, q_1, q_2 \rangle p_3) / \langle q_1, q_2, q_3 \rangle \quad (10)$$

where $\langle q_a, q_b, q_c \rangle$ is the area of the triangle defined by the three points.

Stage-2 of Step-2: Refine the mesh-parameterization based on stretch minimization. After *Stage-1*, the 3D surface mesh is mapped onto a 2D parametric plane, resulting a 2D planar mesh composed of the same number of nodes and triangle elements. The goal of this refinement stage is to change the node coordinates of the 2D planar mesh such that mesh distortion is minimized. Mesh distortion is measured by the average stretch μ, given by

$$\mu = \sqrt{\sum_i A(P_i)\mu_{P_i}^2 / \sum_i A(P_i)} \quad (11)$$

where $A(P_i)$ denote the area of the triangle P_i; μ_{P_i} is the local stretch associated with triangle P_i, and it is defined as

$$\mu_{P_i} = \sqrt{\Gamma^2 + \Upsilon^2} \quad (12)$$

where Γ is max eigenvalue and Γ is the min eigenvalue of the deformation gradient tensor derived from the affine mapping (Eq. 3). We utilize the algorithm proposed by Yoshizawa et al. (2004) to find the optimal node coordinates such that the average stretch μ is minimized. This algorithm has two iteration steps:

(1) Update the node coordinates of the 2D triangle mesh by minimizing the local energy function

$$E = \sum_j a_{i,j} \|q_i - q_j\|^2 \quad (13)$$

In this step, the coefficients $\{a_{i,j}\}$ are fixed. The solution of this minimization problem is found by solving a set of linear equations.

(2) Update each coefficient by using each local stretch

$$a_{i,j} \leftarrow \frac{a_{i,j}}{\mu_{P_j}} \quad (14)$$

The initial values of the coefficients are obtained in *Stage-1*.

After a few iterations, the average stretch μ will be reduced. Then the rectangle region is discretized to a 2D planar quad mesh as shown in Fig. 3c. Using the affine mapping (Eq. 3) each node of the 2D planar quad mesh is transformed to the 3D surface. As a result, the 3D surface is now represented by a quad mesh as shown in Fig. 3d.

References

Alliez P, Ucelli G, Gotsman C, Attene M (2008) Recent advances in remeshing of surfaces. In: De Floriani L, Spagnuolo M (eds) Shape analysis and structuring. Springer, Berlin, pp 53–82

Barrett JF, Keat N (2004) Artifacts in CT: recognition and avoidance. RadioGraphics 24:1679–1691. doi:10.1148/rg.246045065

Bols J, Degroote J, Trachet B, Verhegghe B, Segers P, Vierendeels J (2013) A computational method to assess the in vivo stresses and unloaded configuration of patient-specific blood vessels. J Comput Appl Math 246:10–17

Bommes D, Lévy B, Pietroni N, Puppo E, Silva C, Tarini M, Zorin D (2013) Quad-mesh generation and processing: a survey. Comput Graph Forum 32:51–76

Botsch M, Kobbelt L, Pauly M, Alliez P, Levy B (2010) Polygon mesh processing. A K Peters/CRC Press, Boca Raton

Celi S, Berti S (2014) Three-dimensional sensitivity assessment of thoracic aortic aneurysm wall stress: a probabilistic finite-element study. Eur J Cardiothorac Surg 45:467–475

Chang C-C, Lin C-J (2011) Libsvm: a library for support vector machines. ACM Trans Intell Syst Technol 2:27:21–27:27

Choke E, Cockerill G, Wilson WRW, Sayed S, Dawson J, Loftus I, Thompson MM (2005) A review of biological factors implicated in abdominal aortic aneurysm rupture. Eur J Vasc Endovasc Surg 30:227–244

Coady MA, Rizzo JA, Hammond GL, Mandapati D, Darr U, Kopf GS, Elefteriades JA (1997) What is the appropriate size criterion for resection of thoracic aortic aneurysms? J Thorac Cardiovasc Surg 113:476–491

Cootes TF, Taylor CJ, Cooper DH, Graham J (1995) Active shape models—their training and application. Comput Vis Image Underst 61:38–59

Cortes C, Vapnik V (1995) Support-vector networks. Mach Learn 20:273–297

Davies RR et al (2006) Novel measurement of relative aortic size predicts rupture of thoracic aortic aneurysms. Annal Thorac Surg 81:169–177

Davies RR, Goldstein LJ, Coady MA, Tittle SL, Rizzo JA, Kopf GS, Elefteriades JA (2002) Yearly rupture or dissection rates for thoracic aortic aneurysms: simple prediction based on size. Annal Thorac Surg 73:17–28

Dieleman N, van der Kolk AG, Zwanenburg JJM, Harteveld AA, Biessels GJ, Luijten PR, Hendrikse J (2014) Imaging intracranial vessel wall pathology with magnetic resonance imaging. Circulation 130:192

Doi K (2008) Computer-aided diagnosis in medical imaging: historical review, current status and future potential. Comput Med Imaging Graph 31:198–211

Doyle BJ, Callanan A, Burke PE, Grace PA, Walsh MT, Vorp DA, McGloughlin TM (2009) Vessel asymmetry as an additional diagnostic tool in the assessment of abdominal aortic aneurysms. J Vasc Surg 49:443–454

Elefteriades JA (2008) Thoracic aortic aneurysm: reading the enemy's playbook. Yale J Biol Med 81:175–186

Elefteriades JA, Farkas EA (2010) Thoracic aortic aneurysm clinically pertinent controversies and uncertainties. J Am Coll Cardiol 55:841–857

Erhart P et al (2015) Finite element analysis in asymptomatic, symptomatic, and ruptured abdominal aortic aneurysms: in search of new rupture risk predictors. Eur J Vasc Endovasc Surg 49:239–245. doi:10.1016/j.ejvs.2014.11.010

Fillinger MF et al (2004) Anatomic characteristics of ruptured abdominal aortic aneurysm on conventional CT scans: implications for rupture risk. J Vasc Surg 39:1243–1252

Fillinger MF, Raghavan ML, Marra SP, Cronenwett JL, Kennedy FE (2002) In vivo analysis of mechanical wall stress and abdominal aortic aneurysm rupture risk. J Vasc Surg 36:589–597
Gasser TC (2016) Biomechanical rupture risk assessment: a consistent and objective decision-making tool for abdominal aortic aneurysm patients. AORTA 4:42–60
Gasser TC, Ogden RW, Holzapfel GA (2006) Hyperelastic modelling of arterial layers with distributed collagen fibre orientations. J R Soc Interface 3:15–35
Gee MW, Förster C, Wall WA (2010) A computational strategy for prestressing patient-specific biomechanical problems under finite deformation. Int J Numer Methods Biomed Eng 26:52–72
Georgakarakos E, Ioannou CV, Kamarianakis Y, Papaharilaou Y, Kostas T, Manousaki E, Katsamouris AN (2010) The role of geometric parameters in the prediction of abdominal aortic aneurysm wall stress. Eur J Vasc Endovasc Surg 39:42–48
Ginneken BV, Schaefer-Prokop CM, Prokop M (2011) Computer-aided diagnosis: how to move from the laboratory to the clinic. Radiology 261:719–732
Goodall C (1991) Procrustes methods in the statistical analysis of shape. J R Stat Soc Ser B (Methodol) 53:285–339
Heimann T, Meinzer H-P (2009) Statistical shape models for 3d medical image segmentation: a review. Med Image Anal 13:543–563
Hua J, Mower WR (2001) Simple geometric characteristics fail to reliably predict abdominal aortic aneurysm wall stresses. J Vasc Surg 34:308–315
Liang L, Kong F, Martin C, Pham T, Wang Q, Duncan J, Sun W (2016) Machine learning–based 3-D geometry reconstruction and modeling of aortic valve deformation using 3-D computed tomography images. Int J Numer Methods Biomed Eng 1–13. doi:10.1002/cnm.2827
Lu J, Zhou X, Raghavan ML (2007) Computational method of inverse elastostatics for anisotropic hyperelastic solids. Int J Numer Meth Eng 69:1239–1261
Maier A, Gee MW, Reeps C, Pongratz J, Eckstein H-H, Wall WA (2010) A comparison of diameter, wall stress, and rupture potential index for abdominal aortic aneurysm rupture risk prediction. Ann Biomed Eng 38:3124–3134
Martin C, Sun W, Elefteriades J (2015) Patient-specific finite element analysis of ascending aorta aneurysms. Am J Physiol Heart Circ Physiol 308:1306–1316
Martin C, Sun W, Pham T, Elefteriades J (2013) Predictive biomechanical analysis of ascending aortic aneurysm rupture potential. Acta Biomater 9:9392–9400
Nishimura RA, Otto CM, Bonow RO, Carabello BA, Erwin JP, Guyton RA, O'Gara PT, Ruiz CE, Skubas NJ, Sorajja P, Sundt TM, Thomas JD, ACC/AHA Task Force Members (2014) 2014 AHA/ACC guideline for the management of patients with valvular heart disease: executive summary: a report of the American College of Cardiology/American Heart Association task force on practice guidelines. Circulation 129:2440–2492. doi:10.1161/CIR.0000000000000029
Pham T, Martin C, Elefteriades J, Sun W (2013) Biomechanical characterization of ascending aortic aneurysm with concomitant bicuspid aortic valve and bovine aortic arch. Acta Biomater 9:7927–7936. doi:10.1016/j.actbio.2013.04.021
Pham T, Martin C, Elefteriades J, Sun W (2013) Biomechanical characterization of ascending aortic aneurysm with concomitant bicuspid aortic valve and bovine aortic arch. Acta Biomater 9:7927–7936. doi:10.1016/j.actbio.2013.04.021
Raghavan ML, Ma B, Fillinger MF (2006) Non-invasive determination of zero-pressure geometry of arterial aneurysms. Ann Biomed Eng 34:1414–1419. doi:10.1007/s10439-006-9115-7
Raut SS, Chandra S, Shum J, Finol EA (2013) The role of geometric and biomechanical factors in abdominal aortic aneurysm rupture risk assessment. Ann Biomed Eng 41:1459–1477
Rodríguez JF, Ruiz C, Doblaré M, Holzapfel GA (2008) Mechanical stresses in abdominal aortic aneurysms: influence of diameter, asymmetry, and material anisotropy. J Biomech Eng 130:021023
Ryu C-W, Kwon O-K, Koh JS, Kim EJ (2011) Analysis of aneurysm rupture in relation to the geometric indices: aspect ratio, volume, and volume-to-neck ratio. Neuroradiology 53:883–889
Shum J, Martufi G, Martino ED, Washington CB, Grisafi J, Muluk SC, Finol EA (2011) Quantitative assessment of abdominal aortic aneurysm geometry. Ann Biomed Eng 39:277–286
Simo JC (1987) On a fully three-dimensional finite-strain viscoelastic damage model: formulation and computational aspects. Comput Methods Appl Mech Eng 60:153–173
Staib LH, Duncan JS (1996) Model-based deformable surface finding for medical images. IEEE Trans Med Imaging 15:720–731
Surazhsky V, Surazhsky T, Kirsanov D, Gortler S, Hoppe H (2005) Fast Exact and Approximate Geodesics on Meshes. ACM Trans Graph 24:553–560
Suzuki K (2012) A review of computer-aided diagnosis in thoracic and colonic imaging. Quant Imaging Med Surg 2:163–176
Umeyama S (1991) Least-squares estimation of transformation parameters between two point patterns. IEEE Trans Pattern Anal Mach Intell 13:376–380
Vande Geest JP, Wang DHJ, Wisniewski SR, Makaroun MS, Vorp DA (2006) Towards a noninvasive method for determination of patient-specific wall strength distribution in abdominal aortic aneurysms. Ann Biomed Eng 34:1098–1106. doi:10.1007/s10439-006-9132-6
Vapnik VN (1998) Statistical learning theory. Wiley-Interscience, New York
Venkatasubramaniam AK et al (2004) A comparative study of aortic wall stress using finite element analysis for ruptured and non-ruptured abdominal aortic aneurysms. Eur J Vasc Endovasc Surg 28:168–176
Vorp DA, Raghavan ML, Webster MW (1998) Mechanical wall stress in abdominal aortic aneurysm: influence of diameter and asymmetry. J Vasc Surg 27:632–639
Weisbecker H, Pierce DM, Holzapfel GA (2014) A generalized prestressing algorithm for finite element simulations of pre-loaded geometries with application to the aorta. Int J Numer Methods Biomed Eng 30:857–872
Wittek A, Derwich W, Karatolios K, Fritzen CP, Vogt S, Schmitz-Rixen T, Blase C (2016) A finite element updating approach for identification of the anisotropic hyperelastic properties of normal and diseased aortic walls from 4d ultrasound strain imaging. J Mech Behav Biomed Mater 58:122–138. doi:10.1016/j.jmbbm.2015.09.022
Wittek A, Karatolios K, Bihari P, Schmitz-Rixen T, Moosdorf R, Vogt S, Blase C (2013) In vivo determination of elastic properties of the human aorta based on 4d ultrasound data. J Mech Behav Biomed Mater 27:167–183. doi:10.1016/j.jmbbm.2013.03.014
Wu J, Wang Y, Simon MA, Brigham JC (2012) A new approach to kinematic feature extraction from the human right ventricle for classification of hypertension: a feasibility study. Phys Med Biol 57:7905–7922
Yoshizawa S, Belyaev A, Seidel HP (2004) A fast and simple stretch-minimizing mesh parameterization. In: Proceedings of shape modeling applications, 2004, pp 200–208. doi:10.1109/SMI.2004.1314507